

PAPER

Tunable dynamic moduli of magnetic elastomers: from characterization by x-ray micro-computed tomography to mesoscopic modeling

To cite this article: Giorgio Pessot *et al* 2018 *J. Phys.: Condens. Matter* **30** 125101

View the [article online](#) for updates and enhancements.

Related content

- [Polymer architecture of magnetic gels: a review](#)
Rudolf Weeber, Melissa Hermes, Annette M Schmidt *et al*.
- [Towards a scale-bridging description of ferrogels and magnetic elastomers](#)
Giorgio Pessot, Rudolf Weeber, Christian Holm *et al*.
- [A density functional approach to ferrogels](#)
P Cremer, M Heinen, A M Menzel *et al*.

Tunable dynamic moduli of magnetic elastomers: from characterization by x-ray micro-computed tomography to mesoscopic modeling

Giorgio Pessot¹, Malte Schümann², Thomas Gundermann²,
Stefan Odenbach², Hartmut Löwen¹ and Andreas M Menzel^{1,3} 

¹ Institut für Theoretische Physik II: Weiche Materie, Heinrich-Heine-Universität Düsseldorf, D-40225 Düsseldorf, Germany

² Institute of Fluid Mechanics, Technische Universität Dresden, D-01062, Dresden, Germany

E-mail: menzel@thphy.uni-duesseldorf.de

Received 20 December 2017, revised 5 February 2018

Accepted for publication 12 February 2018

Published 23 February 2018



Abstract

Ferrogels and magnetorheological elastomers are composite materials obtained by embedding magnetic particles of mesoscopic size in a crosslinked polymeric matrix. They combine the reversible elastic deformability of polymeric materials with the high responsivity of ferrofluids to external magnetic fields. These materials stand out, for example, for significant magnetostriction as well as a pronounced increase of the elastic moduli in the presence of external magnetic fields. By means of x-ray micro-computed tomography, the position and size of each magnetic particle can be measured with a high degree of accuracy. We here use data extracted from real magnetoelastic samples as input for coarse-grained dipole-spring modeling and calculations to investigate internal restructuring, stiffening, and changes in the normal modes spectrum. More precisely, we assign to each particle a dipole moment proportional to its volume and set a randomized network of springs between them that mimics the behavior of the polymeric elastic matrix. Extending our previously developed methods, we compute the resulting structural changes in the systems as well as the frequency-dependent elastic moduli when magnetic interactions are turned on. Particularly, with increasing magnetization, we observe the formation of chain-like aggregates. Interestingly, the static elastic moduli can first show a slight decrease with growing amplitude of the magnetic interactions, before a pronounced increase appears upon the chain formation. The change of the dynamic moduli with increasing magnetization depends on the frequency and can even feature nonmonotonic behavior. Overall, we demonstrate how theory and experiments can complement each other to learn more about the dynamic behavior of this interesting class of materials.

Keywords: magnetorheological elastomer, ferrogel, tunable dynamic moduli, dipole-spring model, x-ray microcomputed tomography, structural transition

(Some figures may appear in color only in the online journal)

1. Introduction

One powerful method to devise innovative, enhanced materials is to combine two or more known components into

a new substance featuring new and optimized properties. Among composite materials, magnetoelastic materials such as ferrogels and magnetic elastomers [1–5] blend the elastic, reversible deformability typical of polymeric materials [6, 7] with the responsiveness to external magnetic fields distinctive of ferrofluids [8, 9]. Their possible applications include soft

³ Author to whom any correspondence should be addressed.

actuators [10, 11], tunable vibration absorbers [12, 13], tunable damping devices [14], magnetic field detectors [15, 16], electromagnetic radiation absorbers [17], and smart acceleration sensors [18, 19]. Since the polymer can be bio-compatible, applications for drug delivery [20] have been outlined.

One way to generate soft magnetoelastic materials is to crosslink a polymeric solution in which magnetic particles of mesoscopic size are dispersed. The particles are typically large enough so that they cannot move through the surrounding polymer mesh, or they are directly chemically bound to the polymer network [21–24]. Therefore, when magnetically interacting with an external field and with each other, the particles rotate or push against their environment and in this way deform the surrounding polymer matrix. Thus the resulting ‘magneto-mechanical’ coupling [21, 25, 26] can reversibly change the shape and stiffness of the materials in the presence of an external magnetic field. Consequently, adjusting the magnetic interactions by external magnetic fields, it is possible to tune the mechanical state and properties such as strain [27–31] or elastic moduli [32–40]. This coupling can also influence other physical properties such as resonance frequency [18] or electrical impedance [41]. Furthermore, it is the origin of intriguing features such as formation of chains of magnetic particles [40] and their buckling under magnetic fields [42], superelasticity [43, 44], and complex behaviors of the dynamic moduli [45].

Various theoretical approaches have been performed to describe the behavior of these materials, such as macroscopic theory [15, 26, 46–48], finite-element methods [49–53], as well as discrete particle resolved models [43–45, 54–57]. One new route in the modeling has recently been outlined in the form of a density functional theory [58]. Along these lines, the magnetically induced changes in elastic properties have been described [43–45, 50, 54, 55, 57, 59].

In the particle-resolved approaches, the magnetic particles are usually assumed to carry magnetic point dipoles, a reasonable approximation at low enough volume fractions [60]. The challenge typically consists in representing appropriately the elastic forces mediated by the polymer matrix. To lowest order, the matrix-mediated elastic interaction can be described via linear [45, 57, 61, 62] or nonlinear [63] springs connecting the particles. Other approaches coarse-grain the polymer into a coupled mesh of nearly-incompressible tetrahedra [43, 44], or, conversely, zoom onto the microscopic detail by resolving the individual polymer chains in a coarse-grained way [64, 65]. Within the framework of linear elasticity theory, the matrix-mediated interactions between the particles can be calculated analytically and up to a desired order exactly [66–70].

When devising new materials with smart, enhanced properties, one usually aims at optimizing their response to an external perturbation. For instance, in the case of a vibration absorber, one would like to have a material stiff enough to sustain the required load but also viscous enough to dissipate kinetic energy as quickly as possible. The key physical quantities are the dynamic moduli. They provide the time- or frequency-dependent stress response of the material to an

externally imposed strain. Recently, increasing attention has been paid on investigating the time-dependent properties either via macroscopic [46, 47, 71] or particle-resolving [45, 72, 73] models.

In our previous investigation [45] we outlined a method to compute the frequency-dependent Young and shear moduli $E(\omega)$ and $G(\omega)$, respectively, for basically any given particle arrangement and studied several theoretically assumed particle structures. In the present work, after refining our method, we aim at applying our technique to three-dimensional (3D) particle distributions obtained by x-ray micro-computed tomography (X- μ CT) [40, 74–76] from real experimental samples. We evaluate the dynamic moduli for varying frequencies, volume fractions of magnetic particles, and intensity of the magnetic interactions. Yet, the presented approach is quite general and can, in principle, be applied to other systems as well that feature a finite size with well-defined boundaries, overdamped dynamics, and that can be discretized into a set of individual nodes with mutual potential interactions. In the present context of magnetic elastomers, we assume that the elastic polymer mesh is fine enough so that the embedded magnetic colloidal particles are locked in their positions and cannot move through the polymer network.

Our goal is twofold. On the one hand, mesoscopic models often adopt strong assumptions on the particle arrangement to render the problem manageable [45, 54, 57, 59, 65, 73, 77, 78]. However, depending on the choice of the distribution, this can lead to qualitatively different deformational and stiffening behaviors [45, 54, 57, 59, 78]. Here, we directly use the spatial and size distribution of the particles from real samples the behavior and properties of which we wish to address. On the other hand, we exploit our mesoscopic model to predict, e.g. the dynamic moduli or the stress-strain phase lag, as a function of frequency, deformation geometry, and with increasing magnetic interaction. While our model can be evaluated in a very efficient way together with the internal restructuring under increasing magnetic interactions, it is extremely challenging to measure all these properties simultaneously in experiments.

Our paper is structured as follows. First, in section 2 we present our minimal dipole-spring model including steric repulsion. Then, in section 3, we describe the experimental set-up employed to acquire the particle distributions used as input for our model. Then, our technique to calculate the dynamic moduli is briefly summarized in section 4. Finally, we present our results in section 5 before drawing our final conclusions in section 6.

2. Dipole-spring model

Our employed dipole-spring model is a modified version of the one presented in [45]. First, we summarize the properties of our particle-spring network and explain how it is generated. Then, we discuss the pair potentials acting between the particles and the generated mesh nodes in the reduced units of the system.

2.1. Particle-spring network

We consider a set of N_p spherical magnetic particles with positions $\mathbf{R}_i = (x_i, y_i, z_i)$ and radii a_i ($i = 1, \dots, N_p$). The positions and radii of the magnetic particles are experimentally measured and used as input for our calculation (see section 3 below). Moreover, each particle carries an individual magnetic moment \mathbf{m}_i . We assume an identical magnetization \mathbf{M} for all particles as might be achieved by magnetization in a homogeneous external magnetic field under magnetic saturation or when neglecting mutual particle magnetization. Together with the particle volume $v_{p,i} = \frac{4}{3}\pi a_i^3$ we thus obtain $\mathbf{m}_i = \mathbf{M}v_{p,i}$.

The polymeric network embedding the particles is modeled by a network of harmonic springs. In our previous works we introduced a minimal set of springs directly connecting the particles via Delaunay triangulation [57, 72, 74, 75]. Care was taken to suppress artificial soft shear modes. In the present work, to represent in a better way a uniform elastic background around irregular particle arrangements we insert N_{extra} extra nodes in the space between our magnetic particles. These nodes are non-magnetic, volumeless, and only serve as linking points that connect springs. We similarly label the positions of these mesh nodes by $\mathbf{R}_i = (x_i, y_i, z_i)$, with $i = N_p + 1, \dots, N$. The N_p magnetic particles and the N_{extra} additional nodes add up to a total of $N = N_p + N_{\text{extra}}$ mesh points, implying $3N$ translational degrees of freedom.

The nodes of the total network are initially positioned according to a face-centered-cubic (fcc) lattice. Each lattice site corresponds to a mesh node. The nearest-neighbor connecting edges between the nodes are converted to harmonic springs. Furthermore, a_{mesh} sets the initially identical length of all springs. We choose an appropriately small mesh size comparable to the average interparticle distance in the densest sample, see section 3. In other words, we set our spring network so that it ‘fills’ the gaps between the magnetic particles as homogeneously as possible. Moreover, a_{mesh} is identical for the different investigated systems.

When later an experimentally measured particle configuration of overall cubic shape is imported, it is laid over the spring network. Subsequently, the network node closest to each particle is moved and attached to the center of the particle. We determine the mean square displacement of all these displacements. In a subsequent step, the remaining nodes are stochastically displaced with an identical mean squared displacement, thus randomizing the whole network homogeneously, see figure 1. The lengths of the springs in their undeformed states are adjusted accordingly, so that there are no initial stresses in the elastic network in the absence of magnetic interactions. To maintain an overall cubic shape with well-defined boundaries, the nodes on the outermost layers of the network are, however, only randomized by one fifth of that amount.

It is important to define the boundaries of the resulting configuration, i.e. the faces of the cubic-like system. There are six boundaries: right, left, rear, front, top, and bottom, corresponding, respectively, to the $\pm\hat{x}$, $\pm\hat{y}$, and $\pm\hat{z}$ surfaces. In the following, we will denote the set of particles and nodes belonging to each boundary by $\mathcal{B}_{\hat{\alpha}}$ ($\hat{\alpha} = \pm\hat{x}, \pm\hat{y}, \pm\hat{z}$). The boundaries of our system are chosen in a way to include about

the same number of particles as there are on the faces of the initial fcc network. Later, the magnetized particles will be displaced under increasing magnetization. The particles assigned to the boundaries can change but their overall number remains constant. Below, we will be employing a total of $N = 4631$ nodes. Each boundary comprises about $\sim 5\%$ of them.

Each spring connecting the i th mesh point (particle or extra node) with the j th one is characterized by its elastic constant k_{ij} . We set the elastic constant of each spring to be proportional to its length in the undeformed state. One reason for this choice is that the resulting overall elastic modulus of the whole system should not depend on the artificially introduced length scale a_{mesh} . In our case of a randomized fcc network, we verified numerically that scaling each spring constant proportionally to its length in the undeformed state yields converging moduli for decreasing a_{mesh} . In the case of an infinitely extended regular spring lattice, this result can be derived by analytical arguments [78].

Finally, we assume an overdamped dynamics of our particles and extra mesh nodes [45, 72, 73]. Therefore, the motion of each particle and extra node is subject to an effective frictional force $-c_i\dot{\mathbf{R}}_i$, with the coefficients $c_i = c_0$ identical for each node, both for particles and extra mesh nodes. The reason is that here the relaxation process is mainly determined by the bulk (visco)elastic medium, which, in both cases, is given by the same (visco)elastic polymer. An additional solvent can further modify the dynamic relaxation behavior.

2.2. Pair interactions

We now detail the various contributions to the total energy of the system U . It is composed of elastic U^{el} , magnetic U^{m} , and steric U^{s} contributions such that $U = U^{\text{el}} + U^{\text{m}} + U^{\text{s}}$. First, the elastic energy U^{el} stored in the elastic springs reads

$$U^{\text{el}} = \frac{1}{2} \sum_{i,j=1; i \neq j}^N \frac{k_{ij}}{2} (r_{ij} - \ell_{ij}^0)^2, \quad (1)$$

where the sum runs over all mesh nodes (particles and extra nodes) labeled by i and j ($j \neq i$) and the leading factor $\frac{1}{2}$ ensures that we count each pair interaction only once. Furthermore, $\mathbf{r}_{ij} = \mathbf{R}_j - \mathbf{R}_i$, $r_{ij} = |\mathbf{r}_{ij}|$, and ℓ_{ij}^0 is the length of the spring connecting mesh nodes i and j in the undeformed state. The spring constants are given by $k_{ij} = k_0 \ell_{ij}^0$ (see above), if i and j are connected by a spring, and 0 otherwise. k_0 is then set by the static elastic modulus of the matrix material.

Since we assume the magnetization \mathbf{M} is equal for all particles along an identical direction, set, e.g. by an external magnetic field, the only contribution to the magnetic energy U^{m} due to varying particle distance is the dipole–dipole interaction

$$U^{\text{m}} = \frac{\mu_0}{4\pi} \frac{1}{2} \sum_{i,j=1; i \neq j}^{N_p} \frac{\mathbf{m}_i \cdot \mathbf{m}_j r_{ij}^2 - 3(\mathbf{m}_i \cdot \mathbf{r}_{ij})(\mathbf{m}_j \cdot \mathbf{r}_{ij})}{r_{ij}^5}. \quad (2)$$

Here, the sum runs only over the pairs of the N_p magnetic particles, $\mathbf{m}_i = \mathbf{M}v_{p,i} = \mathbf{M}\frac{4}{3}\pi a_i^3$, and μ_0 is the magnetic permeability of vacuum.

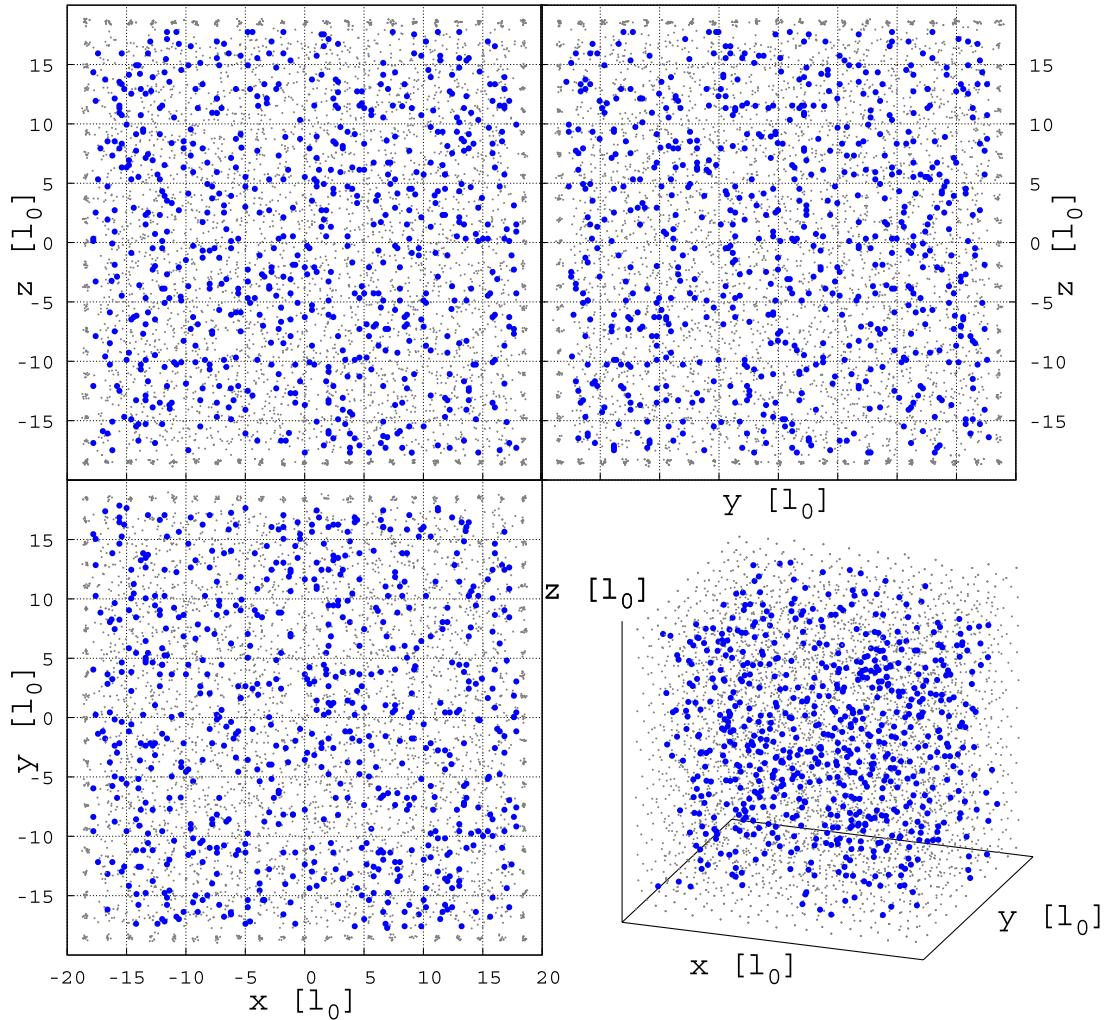


Figure 1. Cartesian projections and 3D plot of magnetic particles (larger, blue spheres) and mesh nodes (smaller, gray spheres) in one numerical realization of an experimental sample. The mesh nodes are numerically generated to represent a homogeneous polymeric matrix. Experimentally, the arrangement of magnetic particles is obtained via X- μ CT (see section 3). A central, homogeneous region of the sample is then cut for the numerical system generation (here of the 40 wt% sample), see section 3.

Finally, the steric repulsion is given by

$$U^s = \frac{1}{2} \sum_{i,j=1; i \neq j}^{N_p} v^s \left(\frac{r_{ij}}{\sigma_{ij}^s} \right), \quad (3)$$

where v^s is a purely repulsive interaction. It is given by

$$v^s(\xi) = \varepsilon^s \left[\xi^{-12} - \xi^{-6} + \varepsilon_c - \frac{c^s}{2} (\xi - \xi_c)^2 \right] \quad (4)$$

for $\xi < \xi_c$ and zero otherwise [45], in the spirit of the WCA [79] potential. The shift ε_c and the cutoff range $\xi_c = 2^{1/6}$ are set to achieve $v^s(\xi_c) = 0$ and $v^{s'}(\xi_c) = 0$. Moreover, the term with the coefficient c^s is introduced to achieve $v^{s''}(\xi_c) = 0$, which requires $c^s = 36 \times 2^{-4/3}$ (see appendix A of [45] for further details). Since we here consider particles of different sizes, we arrange the steric cutoff between particles i and j , where steric interaction sets in, to correspond to the sum of the respective radii. Thus, $\sigma_{ij}^s = 2^{-1/6}(a_i + a_j)$.

To further describe our systems below, we define the characteristic length scale $l_0 = \sqrt[3]{\sum_{i=1}^{N_p} a_i^3 / N_p}$. Thus, the

total volume occupied by the particles is exactly $N_p \frac{4}{3} \pi l_0^3$. Moreover, and as further described in section 3, the distributions of particle radii in the considered samples have similar averages. Thus l_0 is a good length scale to use even when systems of different particle concentration are addressed. We set the strength of our steric interaction to $\varepsilon^s = k_0 l_0^3$.

3. Experimental data acquisition and characteristics of the resulting numerical systems

The experimental samples from which we acquired the particle positions are of cylindrical shape and of weight percentage (weight magnetic particles over sample weight) of 15 and 40 wt%. Manufacturing processes, data acquisition, as well as a comprehensive evaluation of measured particle structures and mechanical properties of the samples are given in [80, 81] (15 wt%), and [40] (40 wt%). In size, the samples had diameters of 3.5 mm and 4 mm as well as heights of 3.5 mm and 5 mm, respectively. To prepare the polymer host matrix, the elastomer kit Elastosil[®] RT 745 A/B (Wacker Chemie AG,

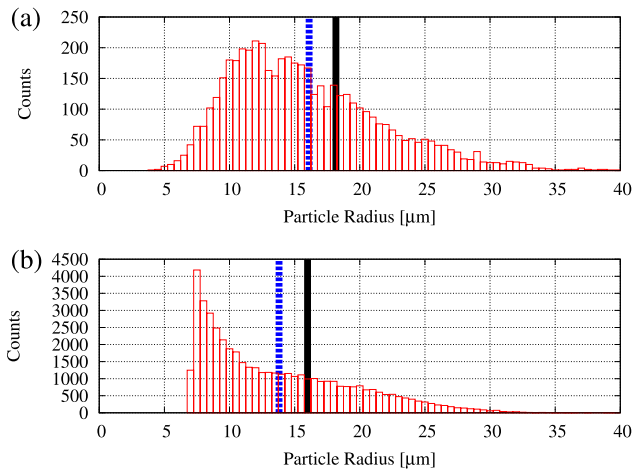


Figure 2. Distribution of radii in μm after converting the irregular shapes of the particles to spheres, maintaining their volumes as provided from the experimental analysis for our (a) 15 wt% and (b) 40 wt% systems. Average radius $\sum_{i=1}^{N_p} a_i/N_p$ and unit length $l_0 = \sqrt[3]{\sum_{i=1}^{N_p} a_i^3/N_p}$ are marked in the plots by the vertical dashed and solid lines, respectively.

Germany) was employed for the sample with 15 wt% and silicone polymers by Gelest Inc. for the sample of 40 wt%.

In both cases, soft-magnetic carbonyl iron powder ASC200 (Höganäs AB, Sweden) was added. The amounts of iron powder of 15 and 40 wt% (volume fraction $\phi \simeq 0.023$ and $\simeq 0.056$) were chosen to obtain significant responsiveness to magnetic fields as well as a statistically significant amount of described particles. On the one hand, the 15 wt% sample was prepared by pouring the silicon-iron powder mixture into a mold which was then immersed into a water bath at 95 °C for two hours for polymerization. On the other hand, the 40 wt% sample was polymerized by action of the catalyst (Alfa Aesar Platinum (0)-1,3-divinyl-1,1,3-tetramethyldisiloxane, 1:20) with a short final phase (30 min at 100 °C) of high-temperature curing to finish. Care was taken to avoid particle sedimentation and to ensure a homogeneous distribution of the particles in the polymerized sample.

In a successive stage, x-ray micro-computed tomography (X- μ CT) scans of the samples were performed. An X- μ CT system [82] with electron current and acceleration voltage set to 170 μA and 90 kV, respectively, was employed. Projected images of the samples were generated by rotating the sample with a 0.25° increment. Furthermore, throughout the CT investigations, temperature remained constant at 20 °C. The exposure time, instead, varied from 2 s to 6.5 s to optimize the quality of the resulting image, for which a magnification factor of 15 was used, thus achieving a resolution of 1 pixel = 3.2 μm . Finally, a self-developed software based on the FDK algorithm [83] was used to reconstruct the 3D images from the projected data. Further processing of the three-dimensional data to obtain the positions and volumes of the particles is performed by a segmentation algorithm using the DIPimage library [84] for matlab.

The experimentally investigated particles had very different, irregular shapes. To handle them effectively in our

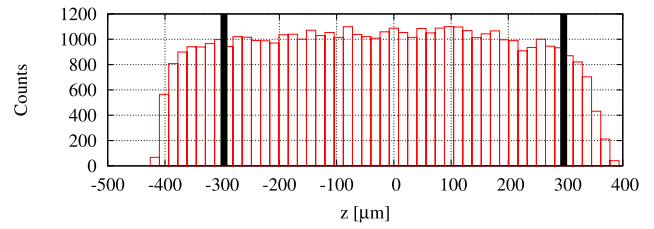


Figure 3. Distribution of the particles along the z -direction in μm for the cylindrical sample of weight fraction 40%. To assure a uniform distribution of magnetic particles we numerically cut a cube from the center of the cylinder as indicated by the vertical lines.

theoretical approach, we converted them to spheres of equivalent volume, which ensures that the overall magnetic dipole moment under saturated magnetization is maintained. The distribution of the resulting radii is shown in figure 2 for the two systems. We note that the detection algorithm for our purpose had to be optimized for positional data, leading to a trade-off concerning the volume data, which does affect the size distributions for the two systems in figure 2. The average radii and average cubed radii show some variations but the extracted radii basically stay within the range of 5–35 μm . Both aspects hinder a quantitative comparison between experiments and theoretical results at the present stage, but good qualitative agreement is achieved.

We choose the z -axis of our Cartesian coordinate system along the cylinder axis. Then, we check the homogeneity of the samples by calculating the particle distribution along the z -direction, see figure 3. As shown in figure 3, the particles are not completely uniformly distributed along the z -direction. Variations are particularly ascribable to slight deviations from perfectly flat boundaries [81]. To work with a distribution of relatively uniform particle density, we use as input of our analysis the magnetic particles contained within a central cube of dimension $\simeq 600$ μm . The distribution of mutual particle distances scaled by the length l_0 is shown in figure 4.

Corresponding data of particle positions and volumes are imported into our numerical algorithm. Then, in both cases a numerical mesh of initial edge length $a_{\text{mesh}} \simeq 2.5l_0$ is generated. The total number of generated mesh nodes is much larger than the number of magnetic particles, see table 1. In the denser sample, we employ $N_{\text{extra}} = 3860$ extra nodes and $N_p = 771$ magnetic particles, for a total of $3N = 3 \times 4631 = 13893$ translational degrees of freedom, as indicated in table 1. This amount of nodes corresponds to a total of 50400 interconnecting springs.

4. Calculation of dynamic moduli

In this section we briefly summarize our extended method to calculate the dynamic moduli. We consider the system initially in equilibrium in the ground state for $\mathbf{M} = |\mathbf{M}| = 0$. As \mathbf{M} increases, the particles reposition from the initial ground state to reduce their magnetic interaction energy U^m until the closest minimum of the total energy U is found, i.e.

$$-\partial_{\mathbf{R}_i} U = \mathbf{F}_i = \mathbf{0}, \quad \forall i = 1, \dots, N. \quad (5)$$

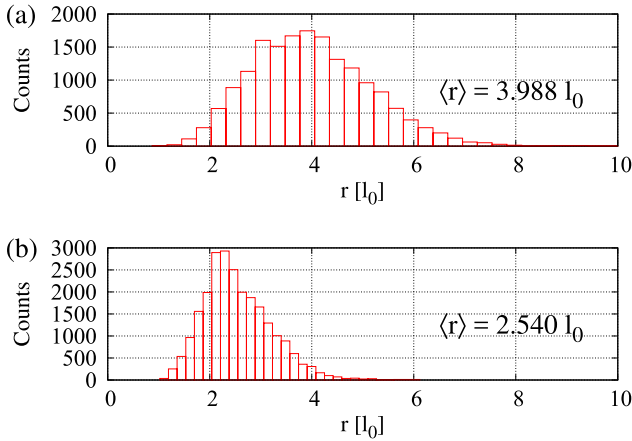


Figure 4. Distribution of the nearest-neighbor distances in our samples of (a) 15 wt% and (b) 40 wt% in terms of scaled particle distances r/l_0 . Particles on the boundaries are excluded from this calculation.

Table 1. For each experimental sample of wt% as indicated we select a cube from its center containing N_p magnetic particles. N_{extra} additional nodes are included in the spring network to achieve a total of $N = N_p + N_{\text{extra}}$ mesh nodes, each with 3 translational degrees of freedom.

wt%	N_p	N_{extra}	N
15%	186	4445	4631
40%	771	3860	4631

This, in general, is achieved at the cost of increasing the elastic and steric energies U^{el} and U^{s} . Because of the large number of degrees of freedom and the irregular particle arrangement, the only practical way to find the equilibrium state is to perform numerical minimization. In the present work, we chose to employ the FIRE algorithm [85]. The control gauge for reaching the equilibrium state is the magnitude of the largest total force acting on a single particle. This means that at convergence no particle is subject to a total force larger than a certain threshold, which we here set to $10^{-3}k_0l_0^2$.

While obtaining the equilibrium configuration, it is crucial to suppress rigid translations and rotations of the whole system. On the one hand, rigid translations induce the system to drift in space and we tackle them by subtracting an identical average from all forces, i.e. by substituting

$$\mathbf{F}_i \leftarrow \mathbf{F}_i - \frac{1}{N} \sum_{j=1}^N \mathbf{F}_j \quad \forall i. \quad (6)$$

Thus, the total force vanishes, $\sum_{i=1}^N \mathbf{F}_i = \mathbf{0}$. On the other hand, a net overall rotation would alter the relative orientation of \mathbf{M} with respect to the system boundaries. Since we here intend to evaluate the moduli for specified geometries and orientations of \mathbf{M} , a global rotation of the system must be averted. For this purpose, we first calculate the instantaneous overall torque $\boldsymbol{\tau} = \sum_{i=1}^N \mathbf{R}_i \times \mathbf{F}_i$. As explained in section 2.1, we model our system as overdamped. Such a torque $\boldsymbol{\tau}$ would then be balanced by the friction resulting from an instantaneous angular rigid rotation $\boldsymbol{\omega} = \mathcal{I}^{-1} \cdot \boldsymbol{\tau}$ of the whole

particle arrangement. \mathcal{I} is a 3×3 auxiliary tensor that has the same structure as the moment-of-inertia tensor, leading to the expression $\mathcal{I} = c_0 \sum_{i=1}^N (\mathbf{R}_i^2 \mathbf{1} - \mathbf{R}_i \mathbf{R}_i)$. \mathcal{I}^{-1} is its inverse, and $\mathbf{1}$ is the unit matrix. To suppress the unrequested rigid rotation at every step of iteration, the force field acting on all the particles is rendered torque-free by subtracting from the force \mathbf{F}_i on each particle i the force $c_0 \boldsymbol{\omega} \times \mathbf{R}_i$, i.e. by substituting

$$\mathbf{F}_i \leftarrow \mathbf{F}_i - c_0 \left(\mathcal{I}^{-1} \cdot \sum_{j=1}^N \mathbf{R}_j \times \mathbf{F}_j \right) \times \mathbf{R}_i \quad \forall i. \quad (7)$$

Then, the total torque vanishes, $\boldsymbol{\tau} = \sum_{i=1}^N \mathbf{R}_i \times \mathbf{F}_i = \mathbf{0}$.

Once the equilibrium positions \mathbf{R}_i^{eq} ($i = 1, \dots, N$) are obtained under a given \mathbf{M} , we can calculate the corresponding dynamic moduli. It is more convenient to treat the problem in terms of deviations from the equilibrium. Therefore, we introduce the displacements $\mathbf{u}_i = \mathbf{R}_i - \mathbf{R}_i^{\text{eq}}$ and their bra-ket notation $|\mathbf{u}\rangle$ to indicate a D -dimensional (here $D = 3N$) vector containing all the degrees of freedom. The key object in this analysis is the Hessian matrix \mathcal{H} of the total energy U . Its elements are given by the second derivative of U with respect to all degrees of freedom, $\mathcal{H}_{ij} = \partial_{u_i} \partial_{u_j} U$. Since the system is in an energetic minimum, U is a convex function of $|\mathbf{u}\rangle$ and \mathcal{H} is positive-semidefinite. We denote eigenmodes and eigenvalues of \mathcal{H} by $|\mathbf{v}_n\rangle$ and λ_n , respectively, so that $\mathcal{H}|\mathbf{v}_n\rangle = \lambda_n|\mathbf{v}_n\rangle$. If the system is subject to a small static external force field $|\mathbf{f}\rangle$ acting on the mesh nodes, its final deformation is determined from the condition $|\mathbf{f}\rangle = \mathcal{H}|\mathbf{u}\rangle$.

To describe external force fields that result in axial or shear deformations, we define external forces acting on the boundary particles. They represent a mechanical stress applied from outside and oriented along preselected directions. In the present work, sticking to the experimental set-up, we focus on axial stretching/compression along the z -direction and shear strains with the shear plane containing $\hat{\mathbf{z}}$ but the force applied perpendicular to it, see figure 5. A corresponding force field must satisfy the following conditions: (i) it is non-vanishing only on the boundaries and oriented in the appropriate directions to build up the corresponding macroscopic stress; (ii) it induces neither translational drift (iii) nor net rotations; and (iv) its magnitude scales with the macroscopic force F corresponding to the stress $\sigma = F/S$ acting on the boundary of surface S .

When a small external force is applied, the system rearranges to balance it and its total energy increases. By decomposing the external force field over the eigenmodes of deformation [42, 45, 72, 86], we can identify the contribution of each mode to the total change in energy. The corresponding static elastic modulus is found as

$$E = \frac{L}{S} \left[\frac{1}{F^2} \sum_{n=1}^D \frac{\langle \mathbf{f} | \mathbf{v}_n \rangle^2}{\lambda_n} \right]^{-1}, \quad (8)$$

where L is the distance between the boundaries on which the forces are applied, calculated from the averaged particle positions in each corresponding boundary. Moreover, the surface S of the boundary $\mathcal{B}_{\hat{\mathbf{z}}}$ is obtained by projecting the nodes and

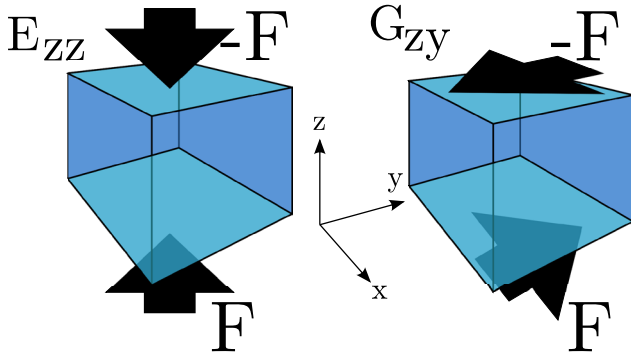


Figure 5. Main geometries to calculate the elastic Young (E_{zz}) and shear (G_{zy}) moduli. The notation E_{zz} indicates that the macroscopic forces are applied onto the $\pm\hat{z}$ surfaces and parallel to the z -direction. In a similar fashion, G_{zy} corresponds to a configuration in which the forces are applied onto the $\pm\hat{z}$ surfaces as well but parallel to the y -direction.

particles belonging to it onto the plane perpendicular to \hat{z} . Subsequently, the convex hull of the projected set of points is determined [87], which allows us to describe samples of non-regular and changing shape.

In the case of a periodically oscillating stress, the former static condition $|\mathbf{f}\rangle = \mathcal{H}|\mathbf{u}\rangle$ becomes an overdamped equation of motion which reads

$$\mathcal{C}|\dot{\mathbf{u}}\rangle(t) + \mathcal{H}|\mathbf{u}\rangle(t) = |\mathbf{f}\rangle(t). \quad (9)$$

The first step consists in transforming it into an eigenvalue problem. The entries of the matrix \mathcal{C} of viscous friction read $\mathcal{C}_{ij} = c_0\delta_{ij}$, with δ_{ij} the Kronecker delta and $i, j = 1, \dots, N$. Since \mathcal{C} and \mathcal{H} commute and can be diagonalized simultaneously, (9) decouples into $D = 3N$ one-variable equations

$$c_0\dot{u}_n(t) + \lambda_n u_n(t) = f_n(t) \quad (10)$$

($n = 1, \dots, 3N$). Each describes the dynamics of a single normal mode, with $u_n(t) = \langle \mathbf{v}_n | \mathbf{u} \rangle (t)$ and $f_n(t) = \langle \mathbf{v}_n | \mathbf{f} \rangle (t)$.

If the time-dependent external force is periodic with a single frequency, i.e. $|\mathbf{f}\rangle(t) = |\mathbf{f}^0\rangle e^{i\omega t}$, then the solution $|\mathbf{u}\rangle(t) = |\mathbf{u}^0\rangle e^{i\omega t}$ of (9) in the steady state will be oscillating with identical frequency, possibly with a time lag. The same is true for the projections onto the normal modes $f_n(t)$ and $u_n(t)$, respectively. Solving for each normal mode in the steady state, we find

$$u_n(t) = u_n^0 e^{i\omega t} = \frac{f_n^0 e^{i\omega t}}{\kappa_n(\omega)} = \frac{f_n(t)}{\kappa_n(\omega)} \quad (11)$$

with $\kappa_n(\omega) = \lambda_n + ic_0\omega$, $u_n^0 = \langle \mathbf{u}^0 | \mathbf{v}_n \rangle$, and $f_n^0 = \langle \mathbf{f}^0 | \mathbf{v}_n \rangle$ [45]. Thus, starting from a given external oscillating force field $|\mathbf{f}^0\rangle e^{i\omega t}$ we can calculate the dynamic linear response of the system in the form $|\mathbf{u}^0\rangle e^{i\omega t}$.

Finally, we define the complex single-frequency dynamic elastic moduli as the ratio between stress and strain in the steady state regime: $E(\omega) = E'(\omega) + iE''(\omega) = \sigma(t)/\varepsilon(t)$. The real and imaginary parts $E'(\omega)$ and $E''(\omega)$ are defined as storage and loss moduli, respectively. To bridge the gap between the macroscopic and the mesoscopic quantities, we identify the total strain of the system as the displacement of the forced boundary particles over the distance between the

forced boundaries, i.e. $\varepsilon(t) = \langle \mathbf{u}(t) | \mathbf{f}^u \rangle / L$. Here, $|\mathbf{f}^u\rangle$ indicates a force field rescaled so that it exerts a total force of unitary magnitude on each boundary in the overall force direction.

The dynamic elastic moduli are then calculated as [45]

$$E(\omega) = \frac{L}{S} \left[\sum_{n=1}^D \frac{f_n^{u2}}{\kappa_n(\omega)} \right]^{-1}, \quad (12)$$

with $f_n^u = \langle \mathbf{v}_n | \mathbf{f}^u \rangle$.

To summarize, we have outlined a procedure that from mesoscopic particle distributions and discretized mesoscopic force fields yields the macroscopic stresses, strains, and elastic moduli. In the following we consider the effect of increasing magnetic interactions on the systems described in section 3. Our main focus will be on the resulting changes in the dynamic elastic moduli.

5. Results

We now investigate how increasing magnetization $M = |\mathbf{M}|$ of the particles affects the overall properties of the system such as internal structure and elastic moduli. In agreement with the experimental set-up, we here set $\mathbf{M} = M\hat{z}$. For the presentation of our results, we measure lengths, energies, forces, and elastic moduli in multiples of l_0 , $k_0 l_0^3$, $k_0 l_0^2$, and k_0 , respectively. Viscosity, velocities, times, and frequencies are measured, respectively, in multiples of c_0/l_0 , $k_0 l_0^2/c_0$, $c_0/k_0 l_0$, and $\omega_0 = k_0 l_0/c_0$. Finally, we measure magnetic moments and magnetization in multiples of $m_0 = \sqrt{4\pi k_0 l_0^6/\mu_0}$ and $M_0 = \sqrt{4\pi k_0/\mu_0}$, respectively.

Since k_0 scales the elastic moduli of the matrix, $M_0 = \sqrt{4\pi k_0/\mu_0}$ gauges the relative strength of elastic and magnetic effects in our reduced units. A magnetoelastomer with elastic modulus of $\sim 10^4$ Pa [33, 40] implies M_0 of the order of $\sim 3 \times 10^5$ A m⁻¹. Since the saturation magnetization of carbonyl iron is $\sim 2 \times 10^6$ A m⁻¹ [88], the range of magnetization would be $M \lesssim 7M_0$. However, applying the rescaled model to very soft gels of elastic moduli ~ 1 Pa [42] suggests up to $M \lesssim 30M_0$ in reduced units.

We consider deformations of the system explicitly involving the magnetization orientation, i.e. the z -direction. Accordingly, we focus on the elastic moduli E_{zz} and G_{zy} , corresponding to axial strain in the z -direction and shear strain with the shear plane containing \mathbf{M} , respectively, as depicted in figure 5.

5.1. Field-induced internal restructuring and chain formation

Increasing the amplitude of the magnetization M , we observe a type of two-step process. First, an initial repositioning of the particles occurs. The initial tendency of dipoles to rotate around each other minimizes their magnetic energy. Next, with increasing M , the dipole-dipole attraction between two magnetic particles can become strong enough to overcome the springs connecting them [61, 89]. Then, in a similar fashion as described in [61] but in a 3D environment, the particles

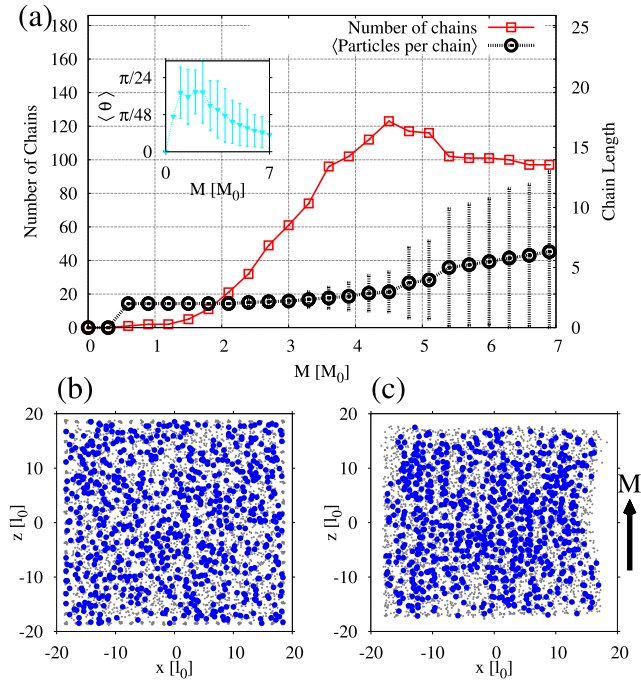


Figure 6. Clustering in one numerical discretization of the 40 wt% sample. Panel (a) shows the number of chains formed for increasing M (left ordinate axis), together with the average number of particles comprised by each chain (right ordinate axis) plotted by solid and dotted lines, respectively. Furthermore, points and bars represent averages and standard deviations over the set of aggregates present in the system. The inset addresses the angle θ between the end-to-end vectors of the chains and \mathbf{M} for increasing M . Panel (b) depicts the projection of extra nodes (light-colored) and magnetic particles (dark-colored) at $M = 0$ onto the xz plane. Panel (c) shows the same plot for the largest M reached in panel (a). There, the formation of chain-like aggregates as well as the overall deformation of the spring network are visible.

collapse towards each other along the \mathbf{M} -direction and are then stabilized by steric repulsion. Consequently, chain-like clusters start to grow, which, initially, consist of just two particles, as depicted in figure 6.

In the following, we identify particles as belonging to the same chain when they are closer than the steric repulsion cutoff distance and caught in a virtually touching state after the dipole–dipole attraction has overcome the connecting elastic springs. When further increasing the magnetization, the distance between particles already in contact changes only slightly due to the strong steric repulsion. For $M \gtrsim 2.5M_0$ chains of more than 2 particles begin to form. After a large enough amount of aggregates has formed, the chains start to merge with each other. This is signaled by a decreasing number of chains for $M \gtrsim 4.5M_0$ while the average chain length keeps increasing.

The formation of the chains is further highlighted by figures 6(b) and (c), which show projections of all nodes onto one plane for $M = 0$ and $M = 7M_0$ of the 40 wt% sample, respectively. By eye, the chain-like aggregates can clearly be identified in figure 6(c). This figure also reveals a limitation of the present basic dipole-spring approach. When the strong internal restructuring occurs in terms of the chain formation, the basic approach cannot provide overall volume

conservation any longer. Therefore, predictions on the absolute lengths resulting for the magnetized sample due to the magnetostrictive behavior [90] are not meaningful in the present context. However, upon chain formation, we still observe on average an increase of the system extension along the field direction relatively to the transversal dimensions. The same is observed in the majority of the experiments in terms of a magnetostrictive elongation along the field direction.

5.2. Dynamic elastic moduli

We now move on to the dynamic Young and shear moduli $E_{zz}(\omega) = E'_{zz}(\omega) + iE''_{zz}(\omega)$ and $G_{xy}(\omega) = G'_{xy}(\omega) + iG''_{xy}(\omega)$ as a function of frequency ω and particle magnetization M . Estimating our reduced unit of measure for the frequency $\omega_0 = k_0 l_0 / c_0$ requires knowledge of the friction coefficient c_0 . Here, we choose a different approach. To compare with experimental data, we match the frequency at which the storage and loss moduli cross as shown in figure 7. At this frequency, $\arctan(E'/E'') = \pi/4$. Comparing with representative rheological measurements [91], we estimate that $\omega_0 \sim 10^3$ Hz for a typical polymeric material of modulus $\sim 10^5$ Pa. Experiments in the low strain regime [91, 92] can explore wide frequency intervals ($10^{-1} - 10^6$ Hz) that in our reduced units would correspond to $10^{-4} - 10^3 \omega_0$.

As explained in section 4, the dynamic moduli, e.g. $E_{zz}(\omega)$, link the macroscopic oscillating stresses and strains, i.e.

$$\sigma_{zz}(\omega) = E_{zz}(\omega)\varepsilon_{zz}(\omega). \quad (13)$$

In the steady-state regime stress and strain both oscillate with the same frequency but shifted by a phase

$$\delta_{zz}(\omega) = \arctan \left[\frac{E''_{zz}(\omega)}{E'_{zz}(\omega)} \right]. \quad (14)$$

Our modeling of the particle dynamics as in (9) corresponds to a Kelvin–Voigt macroscopic model. Such a model is particularly appropriate at longer timescales (i.e. in the small- ω regime). There, it is characterized by a constant storage modulus and a loss modulus that linearly increases with the frequency. Upon decomposition into the normal modes, each mode behaves as an independent Kelvin–Voigt element with different parameters and dynamic modulus $\kappa_n(\omega) = \lambda_n + ic_0\omega$ as in (11). Increasing the oscillation frequency, the dynamic moduli deviate from a simple Kelvin–Voigt description, as shown in figure 7, because the response of the system switches to different combinations of modes.

Data points and bars in figure 7 are obtained from averages and standard deviations of 15 uncorrelated, differently randomized numerical realizations of the spring network. Furthermore, and albeit the Kelvin–Voigt model describes particularly the long-timescale behavior, we here plot for completeness a larger range of ω . We can mainly distinguish between three regimes of frequency.

First, up to $\sim 10^{-2}\omega_0$, the storage moduli have a flat behavior and, in the $\omega \rightarrow 0$ limit, converge to the static elastic moduli. Here the deformation occurs over long timescales and the bulk relaxes completely. Therefore, the storage modulus

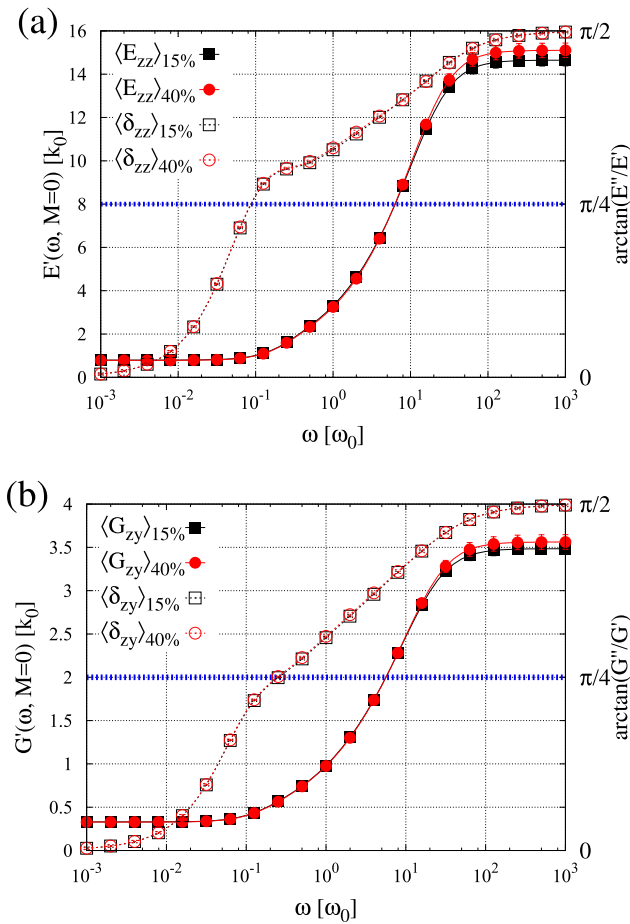


Figure 7. Dynamic (a) Young and (b) shear moduli $E_{zz}(\omega)$ and $G_{zy}(\omega)$ for vanishing magnetic interactions ($M = 0$) for arrangements extracted from samples of 15 and 40 wt%, respectively. The curves for the storage moduli $E'_{zz}(\omega)$ and $G'_{zy}(\omega)$ refer to the left axes. The curves for the phase lags between storage and loss components, (a) $\delta_{zz}(\omega) = \arctan(E''_{zz}/E'_{zz})$ and (b) $\delta_{zy}(\omega) = \arctan(G''_{zy}/G'_{zy})$, refer to the right axes. For $\delta_{zz}(\omega) = \pi/4 = \delta_{zy}(\omega)$ (horizontal dashed blue line) corresponding storage and loss moduli are equal. Data points and bars (where visible) represent averages and standard deviations over 15 different numerical realizations of the spring network surrounding the magnetic particles.

has its minimum with respect to ω . Typically, in experiments the elastic moduli increase with increasing volume fraction ϕ of hard inclusions. According to Einstein's law, $E(\phi) = E(\phi = 0)[1 + 5\phi/2]$ to lowest order in ϕ [93, 94]. Here we do not observe this effect, because we set the springs between the centers of the particles.

The loss moduli in the low- ω regime linearly increase and follow the trend $\sim \eta\omega$, with η an effective viscosity, see figure 8. The viscosities are obtained from the initial slopes of $E''_{zz}(\omega)$ and $G''_{zy}(\omega)$. They are, respectively, $E''_{zz}(\omega)/\omega \sim 10c_0/l_0$ and $G''_{zy}(\omega)/\omega \sim 2c_0/l_0$. In this regime, the phase lags are increasing but small, see figure 7, so that stress and strain are almost completely in phase.

Increasing ω until $\sim 10^{-1}\omega_0$, the phase lags reach the value $\pi/4$, as a consequence of the increasing loss moduli. At this characteristic frequency the storage moduli equal the corresponding loss moduli. As indicated above, this reference

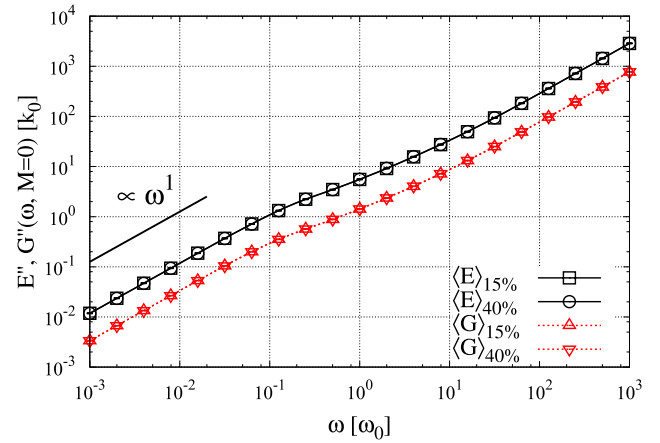


Figure 8. Loss moduli $E''_{zz}(\omega)$ (solid line) and $G''_{zy}(\omega)$ (dashed line) at vanishing magnetization $M = 0$ for samples with 15 and 40 wt%. The double logarithmic scale reveals the initial linear behavior. Data points indicate averages over 15 different numerical realizations of the spring network surrounding the magnetic particles. Standard deviations are much smaller than the symbols.

point could be used to compare our results with experimental measurements.

For increasing frequency ω , the bulk of the system is unable to relax as the oscillation period of the external stress decreases. As a consequence we find an increase in the storage moduli up to $\omega \sim 10^2\omega_0$, where they reach a final plateau. Here, the linear response results from the springs on the boundary and practically no dynamical internal relaxation occurs. The frequency is too large to allow for propagation of the external stimulus into the bulk. In agreement with the Kelvin–Voigt model, the loss moduli keep increasing. Some deviations from the linear increase are visible in the regime $10^{-1}\omega_0 \lesssim \omega \lesssim 10^1\omega_0$, in which the system switches from a low- ω bulk to a high- ω surface response. Subsequently, in the range $\omega \gtrsim 10^2\omega_0$, the phase lags practically reach the stationary value of $\pi/2$, for which stress and strain are completely out of phase. We mention that, at high frequencies, inertial effects may become important. In this case, our results obtained from overdamped dynamics may lose their significance.

5.3. Hardening effects

Increasing the magnetization M of the particles, e.g. by applying an external magnetic field, their spatial arrangement undergoes significant transformations, see figure 6 and section 5.1. Such adjustments are reflected by variations in the elastic moduli.

First we address induced changes in the static moduli $E_{zz}(M)$ and $G_{zy}(M)$, where $E_{zz}(M) = E'_{zz}(\omega = 0, M)$ and $G_{zy}(M) = G'_{zy}(\omega = 0, M)$. For brevity, we denote the moduli at vanishing frequency and magnetization as $E_0 = E'_{zz}(\omega = 0, M = 0)$ and $G_0 = G'_{zy}(\omega = 0, M = 0)$. Moreover, we focus our analysis on the sample with 40 wt% because it shows a stronger response to magnetic interactions. Again we average our results over 15 different numerical realizations of the spring network and show the corresponding

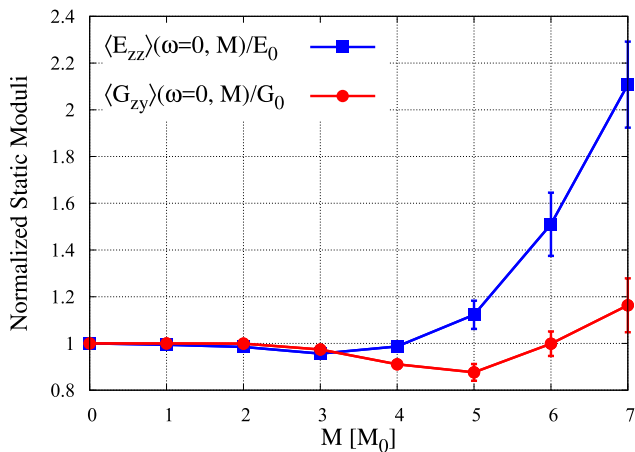


Figure 9. Variation of the static ($\omega = 0$) normalized moduli $E_{zz}(M)/E_0$ and $G_{zy}(M)/G_0$ with increasing magnetization for the sample of 40 wt%. Data points indicate averages over 15 different numerical realizations of the spring network. For $M < 5M_0$ the standard deviations are smaller than those at $M = 5M_0$.

averages and standard deviations. In this way, we link our findings to the specific particle distribution and not to the specific arrangement of the network nodes.

Initially, for $M \lesssim 2M_0$ the moduli do not vary significantly, see figure 9. In this low- M regime, the amount of formed chain-like aggregates is quite small and only few particles are clustered. Furthermore, here the standard deviations on the moduli due to the different realizations of the numerical spring network are less than 1%.

For values of $M \gtrsim 2M_0$ we first observe a slightly decreasing trend for both moduli, more accentuated for the shear modulus which here is reduced by up to 12%. This behavior corresponds to a softening of the systems. Significant particle rearrangements occur in this regime due to the induced magnetic interactions. Apparently, the resulting energetic locking of the corresponding intermediate structures is weaker than in the initial unmagnetized state. Such configurations are, however, stable minima of the system for each given M , as evidenced by the positive values of the moduli.

Finally, for higher $M \gtrsim 4M_0$, we observe a significant increase in both moduli, together with an increase in the statistical standard deviations. We conjecture such a change in behavior to be connected to the structural change in the magnetic particle aggregates, see figure 6. For $M \gtrsim 4M_0$ the clusters of magnetic particles switch from prevalently dimers to longer chain-like aggregates. The corresponding large increase of elastic moduli has previously been predicted theoretically [45] and been observed in experiments [33, 35, 40]. We directly attribute this hardening of the sample to the formation of large chain-like aggregates in the system [61]. They are aligned in the \mathbf{M} -direction and can span large portions of the sample. When the magnetic particles on the chains are at contact in a ‘hardened’ [61] state, they are virtually locked in position by the intense balance of steric and magnetic forces. Each such particle is trapped in a potential well much steeper than the one originating from the spring network. Thus, it is intuitive that the macroscopic deformations illustrated in

figure 5 experience a significant stronger resistance if they work on the hardened chains. Moreover, it is intuitive that the increase in E_{zz} is stronger than the one in G_{zy} in figure 9.

In fact this hardening is certainly one of the most important aspects of the investigated materials in view of practical applications. In magnetic fluids of magnetic colloidal particles suspended in a carrier liquid, external magnetic fields can induce the formation of such chain-like aggregates as well. When this happens, the shear viscosity of the suspension strongly increases, which was, for instance, referred to as ‘magnetoviscous effect’ [95–97]. Here, we apparently observe the analogue to this effect, now for elasticity in solid materials. Comparing figures 6 and 9 with each other, it becomes conceivable that the formation of the chain-like aggregates plays an analogous driving role in the present context.

We now discuss the impact of increasing M on the dynamic moduli. As expected, in the low- ω regime ($\omega \lesssim 10^{-1}\omega_0$) the storage moduli $E'_{zz}(\omega)$ and $G'_{zy}(\omega)$ follow the same behavior as their static counterparts, as shown in figure 10. Moreover, the phase lags δ_{zz} and δ_{zy} in this regime tend to decrease for increasing M . This implies that a large M does not only increase the storage moduli but also helps to keep stress and strain in phase. This is consistent because an increase in, e.g. E'_{zz} directly causes a decrease in $\delta_{zz} = \arctan(E''_{zz}/E'_{zz})$.

For larger $\omega \gtrsim 10^{-1}\omega_0$, a less distinct increase in the storage Young modulus $E'_{zz}(\omega)$ was found. Also the phase lag δ_{zz} is less influenced by the magnetization in this frequency regime. For $\omega \gtrsim \omega_0$ there is no statistically significant variation for δ_{zz} any longer. Interestingly, the storage part of the shear modulus $G'_{zy}(\omega)$ decreases when switching on M at intermediate frequencies ω , in contrast to the low- ω regime. A crossing of the curves for $G'_{zy}(\omega, M=0)$ and $G'_{zy}(\omega, M=7M_0)$ is observed in figure 10. However, for even higher $\omega \gtrsim 10\omega_0$ the storage modulus recovers its increasing behavior with increasing magnetization as in the static case. Approximately, the shear-related phase lag δ_{zy} shows a behavior similar to δ_{zz} , although with smaller amplitudes of variation at intermediate frequencies.

The loss moduli, displayed in figure 11, are influenced by increasing magnetization M as well. Because of the roughly linear behavior in both the low- and high- ω regime, see figure 8, we discuss the variations in terms of changes in $E''_{zz}(\omega)/\omega$ and $G''_{zy}(\omega)/\omega$, which for $\omega \rightarrow 0$ represent the corresponding effective viscosity of the system.

The loss modulus $E''_{zz}(\omega)$ seemingly decreases with increasing M at low to moderate frequencies, thus leading to a reduced effective viscosity. The reason for the larger standard deviations at low frequencies is that the absolute value of $E''_{zz}(\omega)$ vanishes approximately as $E''_{zz}(\omega) \sim \omega$ for $\omega \rightarrow 0$. The same applies to the shear loss modulus $G''_{zy}(\omega)$. While the shear loss modulus $G''_{zy}(\omega)$ always seems to decrease when switching on M , see figure 11(b), the Young loss modulus $E''_{zz}(\omega)$ interestingly changes from decrease to increase for higher frequencies.

The chain formation described in section 5.1 and the stiffenings displayed in figures 9 and 10 can be related to changes in the distribution of the eigenvalues with increasing M , see figure 12. Over the whole range of λ_n , the effect of increasing

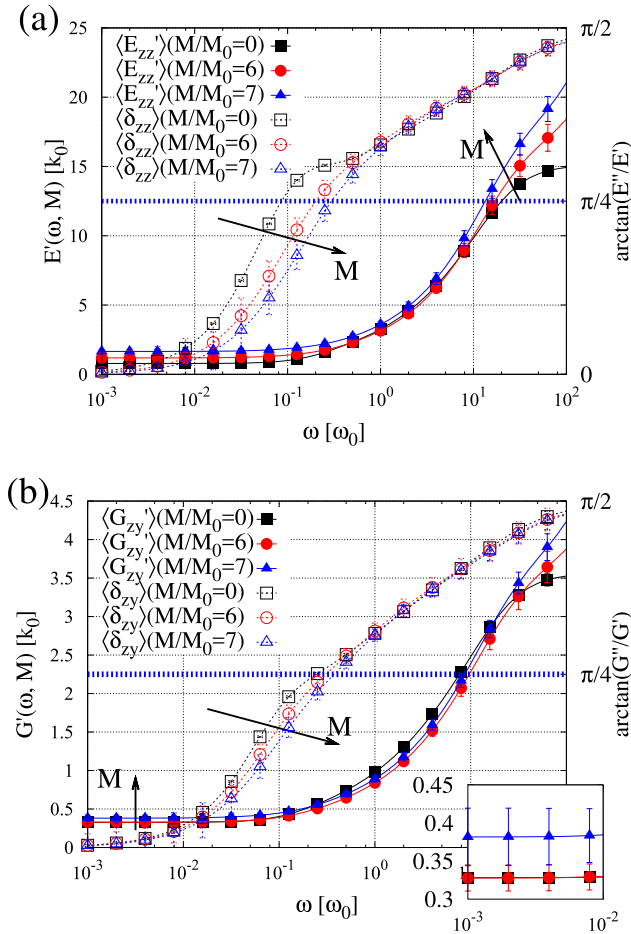


Figure 10. Effect of increasing magnetization M on the storage moduli (a) $E'_z(\omega)$ and (b) $G'_{zy}(\omega)$ (solid lines) as well as on the phase lags (a) $\delta_{zz}(\omega)$ and (b) $\delta_{zy}(\omega)$ (dashed lines) for the 40 wt% sample. The inset in (b) zooms in onto the low- ω behavior of $G'_{zy}(\omega)$, see also figure 9 for the case $\omega = 0$.

M is to lower the smaller ($\lambda_n \lesssim 10k_0l_0$) and to increase the larger ($\lambda_n \gtrsim 10k_0l_0$) eigenvalues. This influence is especially pronounced for the larger λ_n . They correspond to localized normal modes involving nearby particles. Such modes typically dominate the response at high frequencies. The formation of chain-like aggregates strongly magnetically binds the nearby particles to each other, making their relative motion to each other difficult. This explains the significant increase for larger λ_n in figure 12 and is directly reflected by the increase of the storage moduli in figure 10 at high frequencies.

Moreover, the inset of figure 12 reveals an increase in many of the very small eigenvalues λ_n with increasing magnetization M . At low frequencies, the system has time to significantly adjust to the imposed global deformations. Therefore, mainly the more globally extended modes corresponding to long-ranged distortions spanning the system become important in the low- ω regime. Those are especially the modes corresponding to lowest nonvanishing eigenvalues λ_n . Thus, the increase in the elastic storage moduli in figure 10 reflects the increase in these eigenvalues λ_n in the inset of figure 12.

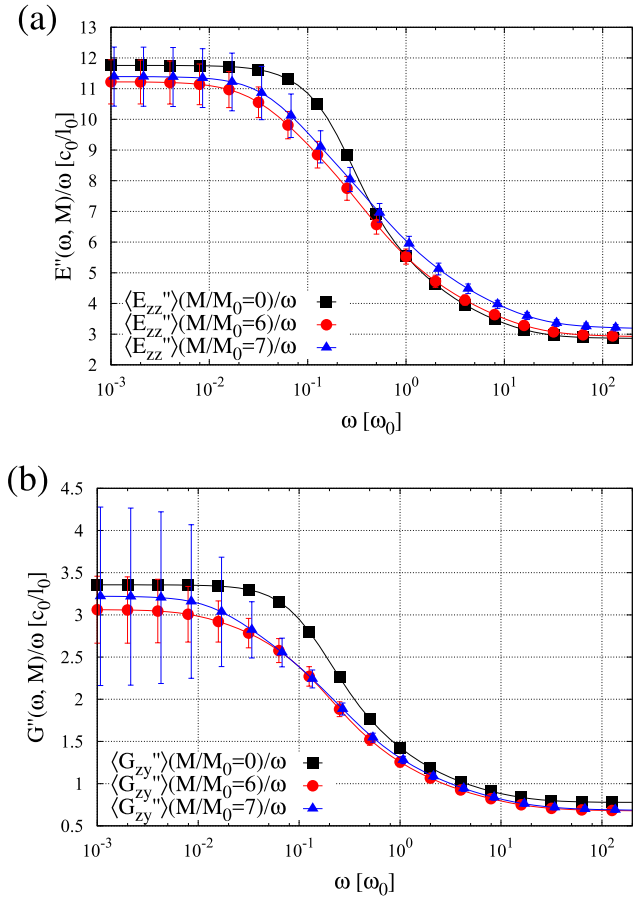


Figure 11. Influence of increasing magnetization M on the loss moduli (a) $E''_z(\omega)$ and (b) $G''_{zy}(\omega)$ for the sample of 40 wt%. Because of the approximately linear increase of the loss moduli with frequency, we here plot them after division by ω .

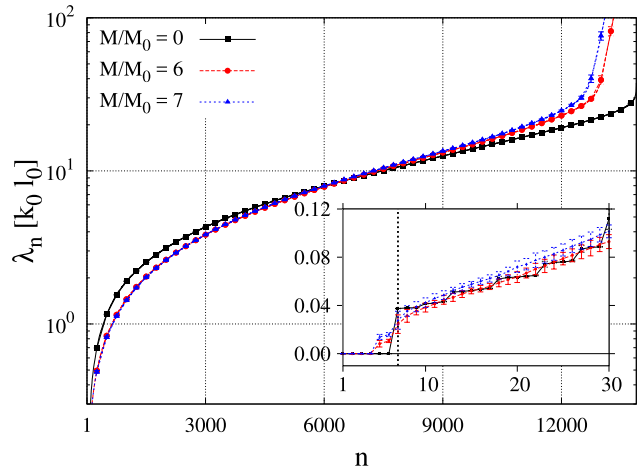


Figure 12. Spectrum of eigenvalues λ_n ($n = 1, \dots, 3N$) for the 40 wt% sample when increasing the magnetization M . Data points and bars correspond to averages and standard deviations, respectively, for 15 different numerical realizations of the spring network. The inset zooms in onto the lowest 31 eigenvalues, while the vertical dashed line separates the 6 lowest λ_n representing 3-dimensional translations and rotations from the other eigenvalues.

6. Conclusions

Bringing together experimental analysis of real samples and the subsequent theoretical and numerical investigation and evaluation of the data can complement the two approaches and increase our understanding of complex materials. Here, refined X- μ CT methods were used to scan macroscopic samples of magnetic elastomers. Mesoscopic information on the positions and volumes of the magnetic particles embedded in an elastic polymeric matrix were obtained this way. The data were collected for different particle concentrations [40, 81]. They are then used as input to an adequately enhanced version of our recent dipole-spring approach [45] of determining the dynamical elastic moduli under varying magnetic interactions.

For this purpose, the elastic polymer matrix in which the particles are embedded is discretized by a randomized network of linear elastic springs. Each magnetic particle forms a node of the resulting elastic network. In addition to that, extra nodes not carrying magnetic particles are included to allow for a more homogeneous elastic network. The particles are assumed of spherical shape, with radii set according to the experimentally measured volumes. For simplicity, when magnetized, e.g. by an external magnetic field, we assume all particles to show the same magnetization. Together with the particle volume, it sets the magnetic dipole moment of each particle that leads to magnetic interactions.

As a consequence of this approach, we can theoretically analyze the competition between magnetic and elastic interactions in the experimental particle arrangement for increasing magnetization. Particularly, this concerns the internal restructuring and the formation of chain-like aggregates [40, 81, 98–100]. Moreover, we can calculate the changes in dynamic elastic storage and loss moduli for increasing magnetization as a function of the frequency of the stress imposed onto the boundaries of the system [45]. Here, we concentrated on a compressive/elongational deformation along the magnetization and a shear deformation containing the magnetization in the shear plane but with boundary displacements perpendicular to it. Switching on the magnetic interactions, we found that the evaluated static elastic moduli first slightly decreased. However, at high magnetization values, we observed the formation of chain-like aggregates in the system, in which the particles are strongly magnetically bound to each other. This leads to significant increase in elastic Young and shear storage moduli at low and high frequencies. Interestingly, a decrease in the elastic shear storage modulus is obtained at intermediate frequencies. Nonmonotonous behavior as a function of frequency, when switching on the magnetization, is also found for the resulting changes in the Young loss modulus. Additionally, we find an increasing magnetization to reduce the out-of-phase lag between the applied stress and the strain response.

As mentioned above, a detailed quantitative comparison between the experimental investigation and theoretical results is not possible at the present stage. However, good qualitative agreement is found with experimental observations accessible so far. Particularly, the formation of chain-like aggregates under increasing magnetization [40, 81] as well as the increase

in the elastic moduli upon chain formation [40] have been reported in the experimental investigations.

On the experimental side, a further improvement of the evaluation algorithm will provide increased precision on the particle positions and volumes. A tracking of the particles for stepwise increase of external magnetic fields and mechanical deformations may further support this effort. Yet, a simultaneous measurement of structure and dynamics will be very challenging using our set-up. However, simultaneously measuring structural changes under deformation and quasi-static stress-strain behavior will provide further insight. We hope that our predictions of the dynamical properties, which are not always easily accessible in experiments, will stimulate further discussions and investigations.

On the theoretical side, an important next task will be to introduce non-spherical particle shapes into the formalism. Moreover, including rotational degrees of freedom [43, 44], surface-bound springs [62], induced dipole effects [60, 101], or many-body elastic interactions [66, 67] will continuously take us towards our goal of combined efforts to study the properties of this class of materials. Furthermore, we could extend our formalism to take into account thermal effects, for instance, by applying stochastic forces to the nodes. In this context, appropriate fluctuation-dissipation relations are necessary [102]. The effect of thermal fluctuations on the overall behavior can be nontrivial [103] and shall be worked out in a broader effort in the future. Spatially inhomogeneous mechanical properties arising, for instance, from inhomogeneous concentrations of the crosslinks or of the embedded rigid particles could be included to some degree by spatial variations of the spring constants. In the longer term, also more sophisticated situations such as deformation or actuation of prestretched states [104] may be addressed.

Altogether, we have presented an approach to quickly estimate for a given sample the internal restructuring and its influence on the macroscopic behavior using the basic but efficient dipole-spring model. For this purpose, for a given piece of material, we need to know as an input the initial particle arrangement, which the x-ray micro-computed tomography can provide. In principle, the experimental analysis could simultaneously provide the data of internal restructuring under magnetization and the effect on the moduli under a given overall static deformation as well. However, each such data acquisition and particularly its evaluation is very time consuming and requires handling of large data files. The dipole-spring approach provides an efficient alternative to evaluate at least the qualitative trends, even if, due to its involved approximations, it is not fully exact quantitatively. Particularly, the dynamic tracking under a given frequency, simultaneously resolving the structural internal changes, seems out of reach at the moment in the experimental analysis, while the dipole-spring approach provides an effective evaluation.

Moreover, to extract a general material behavior and if the details of the statistics for arranging the particles are known, one could quickly generate numerically different realizations of certain particle arrangements in the dipole-spring model, evaluate them, and then average over the results. In this way, an ensemble average would be obtained over

different realizations of the system that could more clearly identify, for instance, transitions in the general behavior of the systems. Experimentally, such a procedure would again be very time consuming and tedious. Still, if, as is the case in the present work, we are interested in the properties of one given piece of material that could be used practically, we have to work with the one given particular realization of this sample, which due to the permanently crosslinked nature of the elastic matrix does not change over the considered time scales. In further integrating the corresponding experimental and theoretical approaches, we aim at an ongoing process of enhancing the tools to develop and design these appealing materials.

Acknowledgments

The authors thank the Deutsche Forschungsgemeinschaft for support of this work through the SPP 1681, grant nos. OD 19/2, PAK 907 (OD 18), LO 418/16, and ME 3571/3.

ORCID iDs

Andreas M Menzel  <https://orcid.org/0000-0003-0713-4979>

References

- [1] Filipcsei G, Csetneki I, Szilágyi A and Zrínyi M 2007 Magnetic field-responsive smart polymer composites *Adv. Polym. Sci.* **206** 137
- [2] Menzel A M 2015 Tuned, driven, and active soft matter *Phys. Rep.* **554** 1
- [3] Lopez-Lopez M T, Durán J D G, Iskakova L Y and Zubarev A Y 2016 Mechanics of magnetopolymer composites: a review *J. Nanofluids* **5** 479
- [4] Odenbach S 2016 Microstructure and rheology of magnetic hybrid materials *Arch. Appl. Mech.* **86** 269
- [5] Cantera M A, Behrooz M, Gibson R F and Gordaninejad F 2017 Modeling of magneto-mechanical response of magnetorheological elastomers (MRE) and MRE-based systems: a review *Smart Mater. Struct.* **26** 023001
- [6] Strobl G 2007 *The Physics of Polymers* (Berlin: Springer)
- [7] Doi M and Edwards S F 1988 *The Theory of Polymer Dynamics* (Oxford: Oxford University Press)
- [8] Odenbach S 2003 Ferrofluids—magnetically controlled suspensions *Colloids Surf. A* **217** 171
- [9] Huke B and Lücke M 2004 Magnetic properties of colloidal suspensions of interacting magnetic particles *Rep. Prog. Phys.* **67** 1731
- [10] Zimmermann K, Naletova V A, Zeidis I, Böhm V and Kolev E 2006 Modelling of locomotion systems using deformable magnetizable media *J. Phys.: Condens. Matter* **18** S2973
- [11] Schmauch M M, Mishra S R, Evans B A, Velev O D and Tracy J B 2017 Chained iron microparticles for directionally controlled actuation of soft robots *ACS Appl. Mater. Interfaces* **9** 11895
- [12] Deng H-X, Gong X-L and Wang L-H 2006 Development of an adaptive tuned vibration absorber with magnetorheological elastomer *Smart Mater. Struct.* **15** N111
- [13] Sun T L, Gong X L, Jiang W Q, Li J F, Xu Z B and Li W H 2008 Study on the damping properties of magnetorheological elastomers based on cis-polybutadiene rubber *Polym. Test.* **27** 520
- [14] Abramchuk S, Kramarenko E, Grishin D, Stepanov G, Nikitin L V, Filipcsei G, Khokhlov A R and Zrínyi M 2007 Novel highly elastic magnetic materials for dampers and seals: part II material behavior in a magnetic field *Polym. Adv. Technol.* **18** 513
- [15] Szabó D, Szeghy G and Zrínyi M 1998 Shape transition of magnetic field sensitive polymer gels *Macromolecules* **31** 6541
- [16] Ramanujan R V and Lao L L 2006 The mechanical behavior of smart magnet-hydrogel composites *Smart Mater. Struct.* **15** 952
- [17] Sedlacik M, Mrlik M, Babayan V and Pavlinek V 2016 Magnetorheological elastomers with efficient electromagnetic shielding *Compos. Struct.* **135** 199
- [18] Volkova T I, Böhm V, Kaufhold T, Popp J, Becker F, Borin D Y, Stepanov G V and Zimmermann K 2017 Motion behaviour of magneto-sensitive elastomers controlled by an external magnetic field for sensor applications *J. Magn. Magn. Mater.* **431** 262
- [19] Becker T I, Zimmermann K, Borin D Y, Stepanov G V and Storozhenko P A 2018 Dynamic response of a sensor element made of magnetic hybrid elastomer with controllable properties *J. Magn. Magn. Mater.* **449** 77
- [20] Zhou M, Liebert T, Müller R, Dellith A, Gräfe C, Clement J H and Heinze T 2015 Magnetic biocomposites for remote melting *Biomacromolecules* **16** 2308
- [21] Frickel N, Messing R and Schmidt A M 2011 Magneto-mechanical coupling in CoFe₂O₄-linked PAAm ferrohydrogels *J. Mater. Chem.* **21** 8466
- [22] Ilg P 2013 Stimuli-responsive hydrogels cross-linked by magnetic nanoparticles *Soft Matter* **9** 3465
- [23] Bose R K, Hohlbein N, Garcia S J, Schmidt A M and van der Zwaag S 2015 Relationship between the network dynamics, supramolecular relaxation time and healing kinetics of cobalt poly(butyl acrylate) ionomers *Polymer* **69** 228
- [24] Landers J, Roeder L, Salamon S, Schmidt A M and Wende H 2015 Particle–matrix interaction in cross-linked PAAm-hydrogels analyzed by Mössbauer spectroscopy *J. Phys. Chem. C* **119** 20642
- [25] Kästner M, Müller S, Goldmann J, Spieler C, Brummund J and Ulbricht V 2013 Higher-order extended FEM for weak discontinuities level set representation, quadrature and application to magneto-mechanical problems *Int. J. Numer. Meth. Eng.* **93** 1403
- [26] Allahyarov E, Menzel A M, Zhu L and Löwen H 2014 Magnetomechanical response of bilayered magnetic elastomers *Smart Mater. Struct.* **23** 115004
- [27] Zrínyi M, Barsi L and Büki A 1996 Deformation of ferrogels induced by nonuniform magnetic fields *J. Chem. Phys.* **104** 8750
- [28] Zrínyi M, Barsi L and Büki A 1997 Ferrogel: a new magneto-controlled elastic medium *Polym. Gels Netw.* **5** 415
- [29] Guan X, Dong X and Ou J 2008 Magnetostrictive effect of magnetorheological elastomer *J. Magn. Magn. Mater.* **320** 158
- [30] Gong X, Liao G and Xuan S 2012 Full-field deformation of magnetorheological elastomer under uniform magnetic field *Appl. Phys. Lett.* **100** 211909
- [31] Varga Z, Filipcsei G, Szilágyi A and Zrínyi M 2005 Electric and magnetic field-structured smart composites *Macromol. Symp.* **227** 123
- [32] Jolly M R, Carlson J D, Muñoz B C and Bullions T A 1996 The magnetoviscoelastic response of elastomer composites consisting of ferrous particles embedded in a polymer matrix *J. Intell. Mater. Syst. Struct.* **7** 613
- [33] Varga Z, Filipcsei G and Zrínyi M 2006 Magnetic field sensitive functional elastomers with tuneable elastic modulus *Polymer* **47** 227

- [34] Stepanov G V, Abramchuk S S, Grishin D A, Nikitin L V, Kramarenko E Y and Khokhlov A R 2007 Effect of a homogeneous magnetic field on the viscoelastic behavior of magnetic elastomers *Polymer* **48** 488
- [35] Kallio M, Lindroos T, Aalto S, Järvinen E, Kärnä T and Meinander T 2007 Dynamic compression testing of a tunable spring element consisting of a magnetorheological elastomer *Smart Mater. Struct.* **16** 506
- [36] Böse H and Röder R 2009 Magnetorheological elastomers with high variability of their mechanical properties *J. Phys.: Conf. Ser.* **149** 012090
- [37] Evans B A, Fiser B L, Prins W J, Rapp D J, Shields A R, Glass D R and Superfine R 2012 A highly tunable silicone-based magnetic elastomer with nanoscale homogeneity *J. Magn. Magn. Mater.* **324** 501
- [38] Borin D Y, Stepanov G V and Odenbach S 2013 Tuning the tensile modulus of magnetorheological elastomers with magnetically hard powder *J. Phys.: Conf. Ser.* **412** 012040
- [39] Schubert G and Harrison P 2016 Equi-biaxial tension tests on magneto-rheological elastomers *Smart Mater. Struct.* **25** 015015
- [40] Schümann M and Odenbach S 2017 *In situ* observation of the particle microstructure of magnetorheological elastomers in presence of mechanical strain and magnetic fields *J. Magn. Magn. Mater.* **441** 88
- [41] Wang Y, Xuan S, Dong B, Xu F and Gong X 2016 Stimuli dependent impedance of conductive magnetorheological elastomers *Smart Mater. Struct.* **25** 025003
- [42] Huang S, Pessot G, Cremer P, Weeber R, Holm C, Nowak J, Odenbach S, Menzel A M and Auernhammer G K 2016 Buckling of paramagnetic chains in soft gels *Soft Matter* **12** 228
- [43] Cremer P, Löwen H and Menzel A M 2015 Tailoring superelasticity of soft magnetic materials *Appl. Phys. Lett.* **107** 171903
- [44] Cremer P, Löwen H and Menzel A M 2016 Superelastic stress-strain behavior in ferrogels with different types of magneto-elastic coupling *Phys. Chem. Chem. Phys.* **18** 26670
- [45] Pessot G, Löwen H and Menzel A M 2016 Dynamic elastic moduli in magnetic gels: normal modes and linear response *J. Chem. Phys.* **145** 104904
- [46] Jarkova E, Pleiner H, Müller H-W and Brand H R 2003 Hydrodynamics of isotropic ferrogels *Phys. Rev. E* **68** 041706
- [47] Bohlius S, Brand H R and Pleiner H 2004 Macroscopic dynamics of uniaxial magnetic gels *Phys. Rev. E* **70** 061411
- [48] Menzel A M 2014 Bridging from particle to macroscopic scales in uniaxial magnetic gels *J. Chem. Phys.* **141** 194907
- [49] Stolbov O V, Raikher Y L and Balasoiu M 2011 Modelling of magnetodipolar striction in soft magnetic elastomers *Soft Matter* **7** 8484
- [50] Han Y, Hong W and Faidley L E 2013 Field-stiffening effect of magneto-rheological elastomers *Int. J. Solids Struct.* **50** 2281
- [51] Metsch P, Kalina K A, Spieler C and Kästner M 2016 A numerical study on magnetostrictive phenomena in magnetorheological elastomers *Comput. Mater. Sci.* **124** 364
- [52] Romeis D, Metsch P, Kästner M and Saphiannikova M 2017 Theoretical models for magneto-sensitive elastomers: a comparison between continuum and dipole approaches *Phys. Rev. E* **95** 042501
- [53] Kalina K A, Brummund J, Metsch P, Kästner M, Borin D Y, Linke J M and Odenbach S 2017 Modeling of magnetic hystereses in soft MREs filled with NdFeB particles *Smart Mater. Struct.* **26** 105019
- [54] Ivaneyko D, Toshchevnikov V P, Saphiannikova M and Heinrich G 2011 Magneto-sensitive elastomers in a homogeneous magnetic field: a regular rectangular lattice model *Macromol. Theor. Simul.* **20** 411
- [55] Wood D S and Camp P J 2011 Modeling the properties of ferrogels in uniform magnetic fields *Phys. Rev. E* **83** 011402
- [56] Weeber R, Kantorovich S and Holm C 2012 Deformation mechanisms in 2D magnetic gels studied by computer simulations *Soft Matter* **8** 9923
- [57] Pessot G, Cremer P, Borin D Y, Odenbach S, Löwen H and Menzel A M 2014 Structural control of elastic moduli in ferrogels and the importance of non-affine deformations *J. Chem. Phys.* **141** 124904
- [58] Cremer P, Heinen M, Menzel A M and Löwen H 2017 A density functional approach to ferrogels *J. Phys.: Condens. Matter* **29** 275102
- [59] Ivaneyko D, Toshchevnikov V, Saphiannikova M and Heinrich G 2012 Effects of particle distribution on mechanical properties of magneto-sensitive elastomers in a homogeneous magnetic field *Condens. Matter Phys.* **15** 33601
- [60] Biller A M, Stolbov O V and Raikher Y L 2014 Modeling of particle interactions in magnetorheological elastomers *J. Appl. Phys.* **116** 114904
- [61] Annunziata M A, Menzel A M and Löwen H 2013 Hardening transition in a one-dimensional model for ferrogels *J. Chem. Phys.* **138** 204906
- [62] Cerdà J J, Sánchez P A, Holm C and Sintes T 2013 Phase diagram for a single flexible Stockmayer polymer at zero field *Soft Matter* **9** 7185
- [63] Sánchez P A, Cerdà J J, Sintes T and Holm C 2013 Effects of the dipolar interaction on the equilibrium morphologies of a single supramolecular magnetic filament in bulk *J. Chem. Phys.* **139** 044904
- [64] Pessot G, Weeber R, Holm C, Löwen H and Menzel A M 2015 Towards a scale-bridging description of ferrogels and magnetic elastomers *J. Phys.: Condens. Matter* **27** 325105
- [65] Weeber R, Kantorovich S and Holm C 2015 Ferrogels cross-linked by magnetic nanoparticles—deformation mechanisms in two and three dimensions studied by means of computer simulations *J. Magn. Magn. Mater.* **383** 262
- [66] Puljiz M, Huang S, Auernhammer G K and Menzel A M 2016 Forces on rigid inclusions in elastic media and resulting matrix-mediated interactions *Phys. Rev. Lett.* **117** 238003
- [67] Puljiz M and Menzel A M 2017 Forces and torques on rigid inclusions in an elastic environment: resulting matrix-mediated interactions, displacements, and rotations *Phys. Rev. E* **95** 053002
- [68] Menzel A M 2017 Force-induced elastic matrix-mediated interactions in the presence of a rigid wall *Soft Matter* **13** 3373
- [69] Kim S and Phan-Thien N 1994 Faxén relations and some rigid inclusion problems *J. Elast.* **37** 93
- [70] Phan-Thien N and Kim S 1994 The load transfer between two rigid spherical inclusions in an elastic medium *Z. Angew. Math. Phys.* **45** 177
- [71] Nadzharyan T A, Sorokin V V, Stepanov G V, Bogolyubov A N and Kramarenko E Y 2016 A fractional calculus approach to modeling rheological behavior of soft magnetic elastomers *Polymer* **92** 179
- [72] Tarama M, Cremer P, Borin D Y, Odenbach S, Löwen H and Menzel A M 2014 Tunable dynamic response of magnetic gels: impact of structural properties and magnetic fields *Phys. Rev. E* **90** 042311
- [73] Ivaneyko D, Toshchevnikov V and Saphiannikova M 2015 Dynamic moduli of magneto-sensitive elastomers: a coarse-grained network model *Soft Matter* **11** 7627
- [74] Günther D, Borin D Y, Günther S and Odenbach S 2012 X-ray micro-tomographic characterization of field-structured magnetorheological elastomers *Smart Mater. Struct.* **21** 015005

- [75] Borbáth T, Günther S, Borin D Y, Gundermann T and Odenbach S 2012 X- μ CT analysis of magnetic field-induced phase transitions in magnetorheological elastomers *Smart Mater. Struct.* **21** 105018
- [76] Gundermann T, Günther S, Borin D and Odenbach S 2013 A comparison between micro- and macro-structure of magnetoactive composites *J. Phys.: Conf. Ser.* **412** 012027
- [77] Ivaneyko D, Toshchevnikov V, Saphiannikova M and Heinrich G 2014 Mechanical properties of magneto-sensitive elastomers: unification of the continuum-mechanics and microscopic theoretical approaches *Soft Matter* **10** 2213
- [78] Pessot G 2017 Coarse-grained discretized description of magneto-responsive elastomers: mesoscopic modeling as a bridge pillar between microscopic simulations and macroscopic behavior *PhD Thesis* Heinrich-Heine-Universität Düsseldorf, Düsseldorf, Germany
- [79] Weeks J D, Chandler D and Andersen H C 1971 Role of repulsive forces in determining the equilibrium structure of simple liquids *J. Chem. Phys.* **54** 5237
- [80] Gundermann T and Odenbach S 2014 Investigation of the motion of particles in magnetorheological elastomers by X- μ CT *Smart Mater. Struct.* **23** 105013
- [81] Gundermann T, Cremer P, Löwen H, Menzel A M and Odenbach S 2017 Statistical analysis of magnetically soft particles in magnetorheological elastomers *Smart Mater. Struct.* **26** 045012
- [82] Shevchenko N, Boden S, Eckert S, Borin D, Heinze M and Odenbach S 2013 Application of x-ray radioscopic methods for characterization of two-phase phenomena and solidification processes in metallic melts *Eur. Phys. J. Spec. Top.* **220** 63
- [83] Feldkamp L A, Davis L C and Kress J W 1984 Practical cone-beam algorithm *J. Opt. Soc. Am. A* **1** 612
- [84] Hendriks C L L, Van Vliet L J, Rieger B, van Kempen G M P and van Ginkel M 1999 DIPimage: a scientific image processing toolbox for MATLAB
- [85] Bitzek E, Koskinen P, Gähler F, Moseler M and Gumbsch P 2006 Structural relaxation made simple *Phys. Rev. Lett.* **97** 170201
- [86] Babel S, Löwen H and Menzel A M 2016 Dynamics of a linear magnetic 'microswimmer molecule' *Europhys. Lett.* **113** 58003
- [87] Jones E *et al* 2001 SciPy: open source scientific tools for Python
- [88] Bombard A J F, Joekes I, Alcántara M R and Knobel M 2003 Magnetic susceptibility and saturation magnetization of some carbonyl iron powders used in magnetorheological fluids *Mater. Sci. Forum* **416** 753
- [89] Stepanov G V, Borin D Y, Raikher Y L, Melenev P V and Perov N S 2008 Motion of ferroparticles inside the polymeric matrix in magnetoactive elastomers *J. Phys.: Condens. Matter* **20** 204121
- [90] Zubarev A Y 2012 On the theory of the magnetic deformation of ferrogels *Soft Matter* **8** 3174
- [91] Zanna J J, Stein P, Marty J D, Mauzac M and Martinoty P 2002 Influence of molecular parameters on the elastic and viscoelastic properties of side-chain liquid crystalline elastomers *Macromolecules* **35** 5459
- [92] Roth M, D'Acunzi M, Vollmer D and Auernhammer G K 2010 Viscoelastic rheology of colloid-liquid crystal composites *J. Chem. Phys.* **132** 124702
- [93] Einstein A 1906 Eine neue Bestimmung der Moleküldimensionen *Ann. Phys.* **324** 289
- [94] Smallwood H M 1944 Limiting law of the reinforcement of rubber *J. Appl. Phys.* **15** 758
- [95] McTague J P 1969 Magnetoviscosity of magnetic colloids *J. Chem. Phys.* **51** 133
- [96] Odenbach S 2004 Recent progress in magnetic fluid research *J. Phys.: Condens. Matter* **16** R1135
- [97] Ilg P, Kröger M and Hess S 2005 Anisotropy of the magnetoviscous effect in ferrofluids *Phys. Rev. E* **71** 051201
- [98] Zubarev A Y, Chirikov D N, Borin D Y and Stepanov G V 2016 Hysteresis of the magnetic properties of soft magnetic gels *Soft Matter* **12** 6473
- [99] Peroukidis S D and Klapp S H L 2015 Spontaneous ordering of magnetic particles in liquid crystals: from chains to biaxial lamellae *Phys. Rev. E* **92** 010501
- [100] Peroukidis S D, Lichtner K and Klapp S H L 2015 Tunable structures of mixtures of magnetic particles in liquid-crystalline matrices *Soft Matter* **11** 5999
- [101] Allahyarov E, Löwen H and Zhu L 2015 A simulation study of the electrostriction effects in dielectric elastomer composites containing polarizable inclusions with different spatial distributions *Phys. Chem. Chem. Phys.* **17** 32479
- [102] Kubo R, Toda M and Hashitsume N 1991 *Statistical Physics II: Nonequilibrium Statistical Mechanics* (Berlin: Springer)
- [103] Xing X, Goldbart P M and Radzihovsky L 2007 Thermal fluctuations and rubber elasticity *Phys. Rev. Lett.* **98** 075502
- [104] Menzel A M, Pleiner H and Brand H R 2009 Response of prestretched nematic elastomers to external fields *Eur. Phys. J. E* **30** 371